Thermal conductivity of the quasi-one-dimensional materials $TaSe_3$ and $ZrTe_3$

Topojit Debnath,* Bishwajit Debnath,† and Roger K. Lake‡
Department of Electrical and Computer Engineering, University of California, Riverside, California 92521, USA

(Received 11 October 2020; accepted 23 February 2021; published 29 March 2021)

The high breakdown current densities and resilience to scaling of the metallic transition-metal trichalcogenides $TaSe_3$ and $ZrTe_3$ make them of interest for possible interconnect applications, and it motivates this paper of their thermal conductivities and phonon properties. These crystals consist of planes of strongly bonded one-dimensional chains more weakly bonded to neighboring chains. Phonon dispersions and the thermal conductivity tensors are calculated using density functional theory combined with an iterative solution of the phonon Boltzmann transport equation. The phonon velocities and the thermal conductivities of $TaSe_3$ are considerably more anisotropic than those of $ZrTe_3$. The maximum longitudinal-acoustic velocity in $ZrTe_3$ occurs in the cross-chain direction, and this is consistent with the strong cross-chain bonding that gives rise to large Fermi velocities in that direction. The thermal conductivities are similar to those of other metallic two-dimensional transition-metal dichalcogenides. At room temperature, a significant portion of the heat is carried by the optical modes. In the low-frequency range, the phonon lifetimes and mean free paths in $TaSe_3$ are considerably shorter than those in $ZrTe_3$. The shorter lifetimes in $TaSe_3$ are consistent with the presence of lower-frequency optical branches and zone-folding features in the acoustic branches that arise due to the doubling of the $TaSe_3$ unit cell within the plane.

DOI: 10.1103/PhysRevMaterials.5.034010

I. INTRODUCTION

The transition-metal trichalcogenides (TMTs) have a quasi-one-dimensional (quasi-1D) crystalline structure that can give rise to quasi-1D behavior of the electronic and phononic properties [1–3]. The lattice structures of TMTs consist of a transition-metal (M) atom, contained at the center of a prism of chalcogen (X) atoms [4]. The MX_3 prisms create strongly M-X covalently bonded chains arranged side by side via longer, weaker M-X bonds, and planarly stacked with even weaker van der Waals-type X-X bonds which effectively makes these materials two-dimensional layers of quasi-1D chains [5], giving them the apt name of quasi-1D materials. The crystalline anisotropy gives rise to directional anisotropy in electrical, optical, phononic, and thermal properties [6–12].

The low dimensionality of the MX_3 materials makes them particularly susceptible to multiple phase transitions, such as superconductivity [13–16] and charge-density wave (CDW) formation [17–20]. The latter has motivated extensive, prolonged research into CDW transitions [1,21–23], sliding [24,25], dynamics [26–30], dimensional scaling [31–38] in the metallic TMTs, and their use for device applications [39–42]. The Fermi-surface nesting, CDW, and their signatures in the phonon spectrum of $ZrTe_3$ are a topic of ongoing interest [43–53]. Inelastic x-ray scattering revealed a Kohn anomaly in the transverse acoustic (TA) phonon of $ZrTe_3$ at the CDW wave vector for temperatures up to 292 K [47]. As the temperature was reduced to and below T_{CDW}, partial Fermi-surface splitting was observed by angle-resolved photoelectron spectroscopy [46,48].

There has been a recent resurgence of interest in 1D and quasi-1D materials, in part, motivated by, and evolving from, the intense interest in two-dimensional (2D) van der Waals materials. Reference [54] provides a review of the more recent work on the transition-metal trichalcogenides. The direct gap semiconductor TiS_3 has received much attention after it was exfoliated to few layer thicknesses and shown to have a high photoresponse with a band gap of 1.1 eV [55]. Investigations of few layer and nanoribbon TiS_3 transistors followed, and experimentally extracted mobilities were in the range of 20–70 $cm^2\,V^{-1}\,s^{-1}$ [9,56–59]. BN encapsulation of 26-nm-thick TiS_3 resulted in two- and four-terminal room-temperature mobilities of 54 and 122 $cm^2\,V^{-1}\,s^{-1}$, respectively [60]. The properties of the MX_3 materials with M = Ti, Zr, and Hf, and X = S, Se, and Te, have been investigated with density functional theory (DFT) to determine electronic structure, band gaps, specific heats, and elastic constants [61]. Exploiting the anisotropy inherent in TMTs has been proposed for application in next generation electronics, contacts, polarizers, and photodetectors [62,63].

The metallic TMTs have also received renewed attention after it was discovered that the breakdown current densities of $TaSe_3$ ($\sim$10 MA/cm^2 where MA represents mega-amperes) and $ZrTe_3$ ($\sim$100 MA/cm^2) are higher than that of Cu [64,65]. Furthermore, in contrast to Cu wires, the resistivity of $TaSe_3$ did not degrade as the cross-sectional dimensions were scaled down to 10 nm [66]. This was attributed to the single-crystalline nature of the nanowires and the self-passivation of the surfaces that eliminate grain-boundary and surface

*tdebn001@ucr.edu
†Current address: Intel Corporation, Hillsboro, Oregon.
‡Corresponding author: rlake@ece.ucr.edu

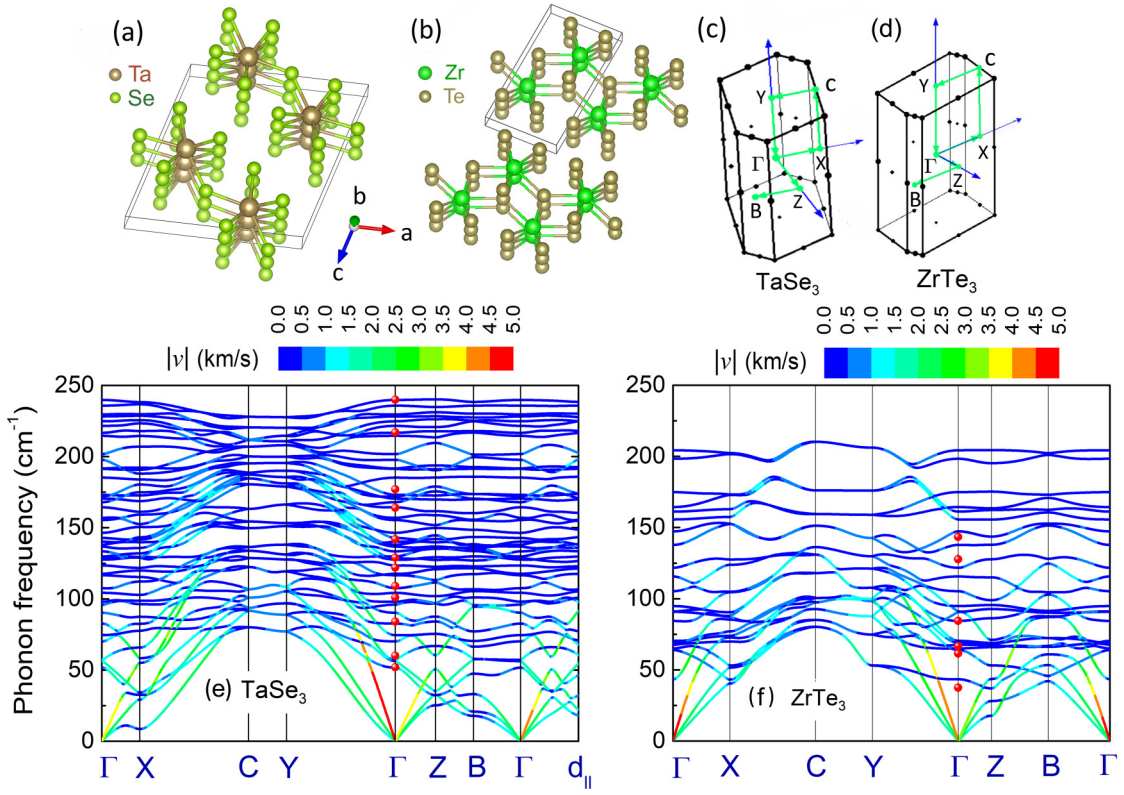

FIG. 1. Crystal structures and unit cells of (a) $TaSe_3$, (b) $ZrTe_3$, and the corresponding Brillouin zones (BZs) for (c) $TaSe_3$ and (d) $ZrTe_3$. The wires grow along the b axis. Lattice vectors a and b lie along the x and y axes, respectively. Lattice vector c lies at angles β with respect to the x axis with values of 106.36° and 97.95° for $TaSe_3$ and $ZrTe_3$, respectively. Phonon dispersions of bulk (e) $TaSe_3$ and (f) $ZrTe_3$. The color indicates the magnitude of the group velocity as given in the color bar. The directions in the Brillouin zone are shown in (c) and (d). The red spheres indicate experimental Raman peaks at 300 K [71,72]. For both crystals, Γ-Y is the chain direction. For $TaSe_3$, Γ-B is the cross-plane direction, and Γ-$d_\parallel$ is the cross-chain direction, where $\mathbf{d}_\parallel = (\mathbf{a}^* + 0.8536\mathbf{c}^*)/2$. For $ZrTe_3$, Γ-Z is the cross-plane direction. Γ-X is 8.0° off from the cross-chain direction, however, the differences in dispersions between the true cross-chain direction and Γ-X are negligible.

roughness scattering. Because of these properties, metallic TMTs were proposed for local interconnect applications in nanoscaled electronics [64,66].

Since the metallic TMTs can carry record current densities and have been proposed for interconnect applications, it is necessary to also understand their thermal transport properties. A secondary motivation to explore the thermal transport properties of low-dimensional materials is their potential of exhibiting higher thermoelectric efficiency [67]. Recently, a high thermoelectric figure of merit was predicted for monolayer $ZrSe_3$ resulting from a high power factor and relatively low thermal conductivity [68].

Although the electronic structure and the electronic transport properties of quasi-1D materials have been extensively studied, their phononic and thermal transport properties have received less attention. Recently, a thermal conductivity of 7 $W\,m^{-1}\,K^{-1}$ was measured in bulk polycrystalline $ZrTe_3$ [69]. A DFT investigation of monolayer $ZrSe_3$ found room-temperature thermal conductivities parallel to the chain direction of 8 $W\,m^{-1}\,K^{-1}$ and perpendicular to the chain direction of 3 $W\,m^{-1}K^{-1}$ [68]. A recent study of TiS_3 found room-temperature thermal conductivities of 5.78 and 2.84 $W\,m^{-1}K^{-1}$ along the chain and interchain directions, respectively [70].

In this paper, we calculate the phonon modes of $TaSe_3$ and $ZrTe_3$ using DFT. We determine the anisotropic velocities of the acoustic branches along the high-symmetry directions, and we compare the frequencies of the optical modes to experimental Raman frequencies and determine the associated mode displacements. We then solve the phonon Boltzmann transport equation (PBTE) to determine the lattice thermal conductivities and to investigate the phonon lifetimes and mean free paths in these two quasi-1D materials.

II. CRYSTALLOGRAPHIC STRUCTURES AND PROPERTIES

Because the TMTs consist of planes of 1D chains of strongly bonded trigonal MX_3 prisms with each chain bonded to its neighbor chain through longer, weaker M-X bonds and each plane bonded to its neighbor plane through even weaker van der Waals-type bonds, we define three different directions: chain, cross-chain (cc), and cross-plane (cp). The chain direction is parallel to the 1D chains and along the **b** lattice vector for both crystals as shown in Fig. 1. The cross-chain direction is perpendicular to the 1D chains and within the same van der Waals plane, and the cross-plane direction is perpendicular to the van der Waals planes.

$TaSe_3$ and $ZrTe_3$ are metallic with monoclinic crystal structures belonging to space-group $P2_1/m$. Both crystals have inversion symmetry so that the phonon modes at Γ have either even or odd parity. The experimentally determined lattice constants of $TaSe_3$ are $a = 10.411$, $b = 3.494$, and $c = 9.836$ Å, and $\beta = 106.36°$; and those of $ZrTe_3$ are $a = 5.895$, $b = 3.926$, and $c = 10.104$ Å, and $\beta = 97.93°$ as shown in Figs. 1(a) and 1(b) [73]. The van der Waals gaps are visible, and the interchain metal-chalcogen bond is longer than the intrachain metal-chalcogen bond. The unit cell of $TaSe_3$ contains 16 atoms, and the unit cell of $ZrTe_3$ contains 8 atoms. The electrical conductivity along the chain direction of $TaSe_3$ at room temperature is reported to be $\sim 1.7 \times 10^5\ (\Omega\,\mathrm{m})^{-1}$ [14], and it remains metallic down to liquid He temperatures [13,14]. $ZrTe_3$ undergoes a CDW phase transition at $T_{CDW} = 63$ K [44,74]. For that reason, we limit our thermal conductivity calculations to temperatures 100 K and above.

The structural and electronic properties of $ZrTe_3$ have been investigated extensively both experimentally and theoretically [44,45,75]. The electrical conductivity of $ZrTe_3$ is highest in the *cross-chain* direction (along the direction of the **a** lattice vector), and, depending on the experimental work, it is a factor of 1.4–1.9 larger than the conductivity in the *chain* direction (along the **b** lattice vector) [45,75]. At $T = 300$ K, experimental values of the electrical conductivity measured along the a axis are $5.6 \times 10^5\ (\Omega\,\mathrm{m})^{-1}$ [75] and $1.3 \times 10^6\ (\Omega\,\mathrm{m})^{-1}$ [45]; and the values measured along the b axis are $4.0 \times 10^5\ (\Omega\,\mathrm{m})^{-1}$ [75] and $6.9 \times 10^5\ (\Omega\,\mathrm{m})^{-1}$ [45]. This is a result of Te-Te σ and σ^* bands formed from Te p_x orbitals. The intrachain Te-Te distance is 2.80 Å, and the cross-chain distance is 3.10 Å allowing for Te-Te bonding that results in highly dispersive electronic bands. We will see a similar anisotropy in the acoustic phonon velocities with the highest velocity also occurring in the *cross-chain* direction.

To investigate the effect of crystal anisotropy, we calculate the phonon dispersions and the acoustic phonon velocities along the chain, cross-chain, and cross-plane directions. The chain direction always corresponds to the $\mathbf{b}^*$ reciprocal lattice vector and the Γ-Y paths in the Brillouin zones shown in Figs. 1(c) and 1(d). For $ZrTe_3$, the cross-chain direction also corresponds to the **a** lattice vector in Fig. 1(b) and the $\hat{x}$ direction in Cartesian coordinates. The cross-plane direction is perpendicular to **a** and, therefore, parallel to the $\mathbf{c}^*$ reciprocal lattice vector. Thus, for $ZrTe_3$, the phonon dispersion in the cross-plane direction is along the Γ-Z path in the Brillouin zone shown in Fig. 1(d). The closest high-symmetry line in the Brillouin zone to the cross-chain direction ($\hat{x}$) is Γ-X and this differs from $\hat{x}$ by 8.0° for $ZrTe_3$. In terms of the reciprocal lattice vectors, the $\hat{x}$ direction for $ZrTe_3$ is $\mathbf{a}^* - 0.2353\mathbf{c}^*$.

For $TaSe_3$, the **a** and **c** lattice vectors have both cross-chain and cross-plane components, and the **a** lattice vector points in the $\hat{x}$ direction. The cross-chain direction is in the direction of the sum of the lattice vectors $\mathbf{a} + \mathbf{c}$ [76]. The cross-plane direction is perpendicular to $\mathbf{a} + \mathbf{c}$ and, therefore, in the direction of $\mathbf{b} \times (\mathbf{a} + \mathbf{c}) \propto (\mathbf{a}^* - \mathbf{c}^*)$ where $\mathbf{a}^*$ and $\mathbf{c}^*$ are the reciprocal lattice vectors on the x-y plane. Thus, for $TaSe_3$, the phonon dispersion in the cross-plane direction is along the Γ-B path in the Brillouin zone shown in Fig. 1(c). The closest high-symmetry line in the Brillouin zone to the cross-chain direction is along $\mathbf{a}^* + \mathbf{c}^*$ which runs between Γ and the corner of the X and Z faces in Fig. 1(c). This differs from the true cross chain direction by 3.4°. The true cross chain direction is $\mathbf{a}^* + 0.8536\mathbf{c}^*$.

III. METHODS

Structural optimization of each material is performed using density functional theory with the projector-augmented-wave method [77] and Perdew-Burke-Ernzerhof exchange-correlation functionals [78] as implemented in the Vienna *ab initio* simulation package [79,80]. The van der Waals interactions are included by semiempirical correction of Grimme-D2 [81]. Converged Monkhorst-Pack grids of $9 \times 9 \times 3$ are used for $TaSe_3$ and $ZrTe_3$. All structures are relaxed until the forces on each atom is less than 10^{-5} eV/Å and the energy convergence reaches 10^{-8} eV. The relaxed lattice constants of $TaSe_3$ and $ZrTe_3$ are within 1% of the experimentally reported values. The magnitudes and angles are provided in the Appendix along with the calculated electronic dispersions.

To obtain the phonon frequency dispersion and other thermodynamics properties, the second-order (harmonic) interatomic force constants (IFCs) are required. The second-order IFCs are calculated using the finite-displacement supercell approach as implemented in PHONOPY [82,83]. For the phonon dispersion of $TaSe_3$ and $ZrTe_3$, a supercell size of $2 \times 2 \times 2$, has been used with a K-point grid of $2 \times 6 \times 2$ and $6 \times 6 \times 4$, respectively.

The thermal conductivity tensor is calculated from the phonon Boltzmann transport equation, within the three-phonon scattering approximation as implemented within ShengBTE [84,85],

$$\kappa_{\alpha\beta} = \frac{1}{k_B T^2 N V} \sum_{\lambda} f_\lambda^0 \left(f_\lambda^0 + 1\right) (\hbar\omega_\lambda)^2 v_\lambda^\alpha F_\lambda^\beta. \qquad (1)$$

In Eq. (1), ω_λ is the phonon energy of each phonon mode λ, f_λ^0 is the equilibrium Bose-Einstein distribution of that mode, and v_λ is the group velocity. λ represents both phonon branch index p and wave-vector $\mathbf{q}$. V is the volume, and N is the number of $\mathbf{q}$ points in the irreducible Brillouin zone. The quantity $F_\lambda^\beta = \tau_\lambda^0 (v_\lambda^\beta + \Delta_\lambda^\beta)$ where τ_λ^0 is the lifetime in the relaxation-time approximation (RTA), and Δ_λ^β is a correction to the RTA from an iterative solution of the PBTE. Full details of the theory are described in Ref. [84]. Diagonal elements of κ along other directions are obtained by a unitary transformation (rotation) of the thermal conductivity tensor.

The calculation of the three-phonon matrix elements, needed for the calculation of τ_λ^0 and Δ_λ^β [84], requires the third-order (anharmonic) IFCs. A $2 \times 2 \times 1$ supercell is used to calculate the anharmonic IFCs, which generates 3472 and 520 atomic structure configurations for $TaSe_3$ and $ZrTe_3$, respectively. Atomic interactions up to fifth-nearest neighbor are considered. Both the RTA and the full iterative approach are used to solve the phonon BTE as implemented in the SHENGBTE package [84,86]. In the iterative approach, κ is converged to a precision of 10^{-5} between iterative steps. Convergence with respect to the k-point grid is also checked. The converged Monkhorst-Pack grids are $14 \times 14 \times 6$ for $TaSe_3$ and $8 \times 14 \times 8$ for $ZrTe_3$.

TABLE I. Velocity (m/s) of LA and TA modes near Γ along four high-symmetry directions and the exact cross-chain direction labeled as $\mathbf{d}_{cc}$. The chain direction is Γ-Y. The cross-plane direction is Γ-B for $TaSe_3$ and Γ-Z for $ZrTe_3$. The first row for each mode corresponds to the velocities at Γ. If the maximum velocity occurs at finite frequency, its value and corresponding frequency (cm^{-1}) are provided in the second row. A "–" in the rows indicates that the maximum velocity occurs at Γ.

Material	Mode	Γ-X	Γ-Y	Γ-Z	Γ-Z	$\mathbf{d}_{cc}$
$TaSe_3$	LA	3962	4956	3814	2342	4105
	TA_1	1558	1256	2000	1467	1824
		–	2143 (35.6)	–	–	–
	TA_2	2374	2294	2446	1963	2481
		–	2409 (38.0)	–	–	–
$ZrTe_3$	LA	4723	4343	3256	4686	4734
	TA_1	1618	1629	1562	1634	1511
		–	1829 (23.1)	–	1651 (13.5)	–
	TA_2	2127	2406	2257	2391	2081
		–	2563 (37.4)	–	–	–

IV. RESULTS AND DISCUSSIONS

A. Phonon dispersion

The phonon dispersions of $TaSe_3$ and $ZrTe_3$ are shown in Figs. 1(e) and 1(f). The color scheme indicates the absolute group velocity at each phonon $\mathbf{q}$ vector and phonon branch with the magnitudes given by the color bars. The large number of atoms in the unit cells result in many low-frequency optical modes. A number of the optical modes are highly dispersive. Experimentally, the many optical modes create complex Raman spectra with closely spaced peaks. The red circles indicate the peaks from experimental Raman data [71,72]. Most of the experimental Raman peaks match well with the DFT calculated phonon frequencies at Γ as shown in Figs. 1(e) and 1(f). The experimental and calculated values are listed in the Supplemental Material (SI) [87] along with images of the displacements and symmetry of each mode at Γ. Below, we first discuss the anisotropy of the acoustic modes, and then we discuss the nature of several of the lower-frequency dispersive optical modes.

The anisotropy of the transition-metal trichalcogenides has been a topic of long-term interest. The degree with which a crystal behaves as quasi-1D or quasi-2D depends on the strength of the interchain coupling, and the interchain coupling manifests itself in the directional dispersions of both the electrons and the phonons. Larger coupling results in more dispersive bands and higher velocities. Thus, the phonon velocities give one measure of the anisotropy of the crystals. The velocities of the three acoustic modes along four high-symmetry lines of the Brillouin zone and the exact cross-chain direction are given in Table I.

For these crystals, the LA velocities along the chain directions (Γ-Y) are high, and for $TaSe_3$, they are the maximum velocities among all modes and all directions as one would expect from a quasi-1D crystal structure. For $ZrTe_3$, the highest velocity phonon is the LA mode in the *cross-chain* direction. This is consistent with its electronic anisotropy in which the highest Fermi velocities occur for the Te p_x bands in the cross-chain direction (electronic structure plots are shown in the Appendix).

The maximum velocities of the TA shear modes are highest along the chain directions for these crystals with the one exception of the TA_2 mode of $TaSe_3$ which has its highest velocity in the cross-chain direction. Also, there is more nonlinearity to the TA mode dispersions such that the maximum velocities of the TA modes occur at a finite frequency on the order of 1 THz.

Finally, the lowest velocity LA modes for both crystals are in the cross-plane direction. For $TaSe_3$, the lowest velocity TA modes are also in the cross-plane direction, and for $ZrTe_3$, the lowest velocity TA modes are in the cross-chain direction.

The acoustic phonon velocities exhibit different degrees of anisotropy for these two crystals. If we consider, for example, the LA mode, then its anisotropy in $TaSe_3$ is significantly larger than in $ZrTe_3$. For $TaSe_3$, the ratios of the maximum velocities in the chain (v_y), cross-chain (v_{cc}), and cross-plane (v_{cp}) directions are $v_y/v_{cc} = 1.2$, $v_y/v_{cp} = 2.1$, and $v_{cc}/v_{cp} = 1.8$. For $ZrTe_3$, the ratios are $v_{cc}/v_y = 1.09$, $v_{cc}/v_{cp} = 1.8$, and $v_y/v_{cp} = 1.3$. Every ratio in $TaSe_3$ is greater than or equal to the corresponding one in $ZrTe_3$. The LA mode of both materials appears to be more quasi-two dimensional rather than quasi-one dimensional since the in-plane anisotropy as characterized by the ratio v_y/v_{cc} or v_{cc}/v_y is considerably less than the cross-plane anisotropy as characterized by the ratios v_y/v_{cp} and v_{cc}/v_{cp}. The anisotropy of the maximum velocities of the TA modes is always less than that of the LA modes. For example, in $TaSe_3$, the TA_1 velocity ratios are $v_y/v_{cc} = 1.2$, $v_y/v_{cp} = 1.5$, and $v_{cc}/v_{cp} = 1.2$; and the TA_2 ratios are $v_{cc}/v_y = 1.03$, $v_{cc}/v_{cp} = 1.3$, and $v_y/v_{cp} = 1.2$.

We now consider the optical modes. The vibrational modes of $TaSe_3$, shown in Fig. 1(e), can be represented at Γ as [71]

$$\Gamma_{TaSe_3} = 8A_u + 8B_g + 16B_u + 16A_g. \quad (2)$$

The $8A_u + 8B_g$ modes have vibrations along the chain axis (b axis), and the $16B_u + 16A_g$ modes are polarized on the **a**-**c** plane. Illustrations of the displacements of the modes based on the point-group symmetry of the isolated chains are shown in Ref. [88]. For each mode at Γ, the frequency, symmetry, and images of the displacements calculated for the periodic

unit cell are provided in the SI [87]. The measured Raman frequency taken from the literature is also listed for each A_g and B_g mode.

Relevant to thermal transport, there are several low-frequency optical modes that have relatively large dispersion along the chain (Γ-Y) direction with maximum velocities in the range of 1–1.5 km/s. The three low-frequency optical modes with the largest dispersions (highest velocities) are B_g or A_u modes with displacements along the chain direction. Modes 5 (56.3 cm^{-1}) (B_g), 6 (57.1 cm^{-1}) (A_u), and 8 (74.5 cm^{-1}) (B_g) at Γ (counting upwards from zero frequency) are examples of such modes. Mode 4 (52.0 cm^{-1}, A_g) with displacements in the a-c plane is slightly less dispersive immediately near Γ, but it has a relatively constant velocity of ∼1 km/s along the entire Γ-Y line. Above 75 cm^{-1}, the longitudinal acoustic mode appears to hybridize with many optical modes resulting in significant dispersion along Γ-Y for modes between 75 and 130 cm^{-1}.

The other types of optical modes are the A_g and B_u modes with either rotation- or libration-type noncollinear displacements on the a-c plane perpendicular to the 1D chains. The fourth (51.7 cm^{-1}) (A_g), seventh (70.2 cm^{-1}) (A_u), and ninth (82.7 cm^{-1}) (A_g) modes at Γ correspond to such modes. In mode 4, each half of the unit cell on either side of the van der Waals gap has a rotational-type displacement, and the rotational displacements of each half are out of phase by 180°. This is typical of all of the rotational-type A modes with displacements in the **a**-**c** plane.

Figure 1(f) shows the phonon dispersion of $ZrTe_3$. For $ZrTe_3$, there are 24 vibrational modes which can be represented at Γ as [72]

$$\Gamma_{ZrTe_3} = 4A_u + 4B_g + 8B_u + 8A_g. \quad (3)$$

Similar to $TaSe_3$, the displacements of the $4A_u + 4B_g$ modes have vibrations along the chain (b) axis, and the $8B_u + 8A_g$ modes have displacements in the a-c plane. There are four optical modes with relatively large dispersions along the chain (Γ-Y): modes 5 (64.0 cm^{-1}, B_g), 8 (69.1 cm^{-1}, B_g), 9 (70.4 cm^{-1}, A_g), and 12 (91.1 cm^{-1}, A_g). For $ZrTe_3$, both types of displacements give rise to these relatively high velocity optical modes. Modes 5 and 8 have displacements along the chain, and modes 9 and 12 have displacements in the a-c plane. Between 75 and 110 cm^{-1}, hybridization occurs between the longitudinal acoustic mode and the optical modes resulting in significant dispersion of the modes in that frequency window.

Although the highest velocity acoustic mode is in the cross-chain (Γ-X) direction, there are fewer dispersive optical modes along Γ-X than in the chain direction. For this reason, the thermal conductivity is highest in the chain direction since, as we will see, a significant proportion of the heat is carried by the optical modes.

B. Thermal conductivity

Figure 2 shows the lattice thermal conductivity for $TaSe_3$ and $ZrTe_3$ calculated from the PBTE using the full iterative approach. The iterative approach gives values slightly higher than those from the relaxation-time approximation, and a comparison of the results from the two approaches is given in the Appendix. Below, we discuss the magnitudes and anisotropies of the thermal conductivities using the T = 300 K values shown in Fig. 2. The lattice thermal conductivities in the chain directions (κ_{yy}) of $TaSe_3$ and $ZrTe_3$ are 6.15 and 9.57 $Wm^{-1}K^{-1}$, respectively. These values are similar to those of other metallic 2D TMD materials as shown in Table II. The calculated lattice thermal conductivities of $TaSe_3$ and $ZrTe_3$ follow a T^{-1} dependence expected when the thermal conductivity is limited by three-phonon scattering [90]. The diagonal elements of κ are fitted to the function $c_1 + c_2T^{-1}$, and the values of the coefficients are tabulated in the Appendix. The root-mean-square errors of all fits to the numerical data are less than 3×10^{-15} $W\,m^{-1}\,K^{-1}$.

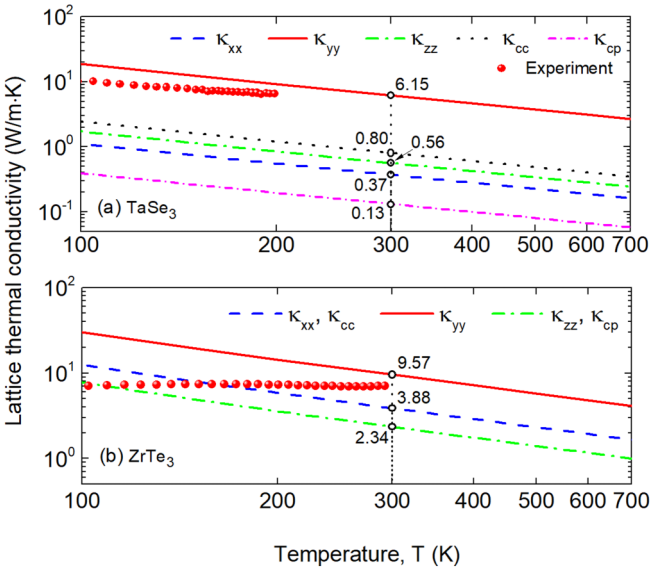

FIG. 2. The three diagonal components of the lattice thermal conductivity tensor versus temperature for (a) $TaSe_3$ and (b) $ZrTe_3$. For $TaSe_3$, the diagonal components of the transformed thermal conductivity tensor in the cross-chain (κ_{cc}) and cross-plane (κ_{cp}) directions are also shown. For $ZrTe_3$, $\kappa_{cc} \equiv \kappa_{xx}$, and $\kappa_{cp} \equiv \kappa_{zz}$. The various components are indicated by the legends. The values for T = 300 K are labeled on the plots in units of $W\,m^{-1}\,K^{-1}$. The red circles are experimental thermal conductivity values for (a) $TaSe_3$ and (b) polycrystalline $ZrTe_3$ taken from the literature [69,89].

The anisotropy of the thermal conductivity in $TaSe_3$ as indicated by the ratios $\kappa_{yy}/\kappa_{cc} = 7.7$ and $\kappa_{yy}/\kappa_{cp} = 47$ is large. For $ZrTe_3$, the anisotropy given by the ratios $\kappa_{yy}/\kappa_{cc} = 2.5$ and $\kappa_{yy}/\kappa_{cp} = 4.1$ is considerably less. Unlike the electrical conductivity which is maximum in the cross-chain direction, the thermal conductivity of $ZrTe_3$ is maximum in the chain direction, even though the maximum phonon velocity occurs at very low frequencies for the LA mode in the cross-chain direction.

The experimental reports of thermal conductivity of quasi-1D materials are rare due to the difficulty in measuring the thermal conduction in such ribbonlike geometries [89]. To our knowledge, only one experimental study of the thermal conductivity of $TaSe_3$ has been reported using a parallel thermal conductance (PTC) technique [91], and the data points are shown in Fig. 2(a) [89]. The experimental values are lower than the calculated values, and the comparison improves

TABLE II. Thermal conductivities from this paper and from the literature.

Type	Materials	Thermal conductivity ($W\,m^{-1}\,K^{-1}$)	Remarks	Reference
	$TaSe_3$	6.2, 0.80, 0.13	Chain, cross-chain, and cross-plane directions	This paper
	$ZrTe_3$	9.6, 3.9, 2.3	Chain, cross-chain, and cross-plane directions	This paper
	$TaSe_3$	4.8	Experimental result (extrapolated to 300 K)	[89]
	$NbSe_3$	24	Bulk material	[99]
Quasi-1D	TiS_3	5.8, 2.8	Chain and cross-chain directions	[70]
	$ZrTe_3$	7	Bulk polycrystalline	[69]
	$ZrTe_5$	11.2	Bulk material	[100]
	$ZrTe_5$	3.9, 1.9, 0.4	Chain, cross-chain, and cross-plane directions	[101]
	$ZrTe_5$	2.2	Bulk polycrystalline	[102]
	HfS_2	9	First-principles study	[103]
	$HfSe_2$	8	First-principles study	[103]
	MoS_2	1	Pristine	[104]
	$MoSe_2$	0.9	Pristine	[104]
	$MoSe_2$	2.3	Compacted polycrystalline	[105]
	$MoTe_2$	1.9	Compacted polycrystalline	[105]
	NbS_2	11.8	Bulk material	[106]
	$NbSe_2$	2.1	Compacted polycrystalline	[105]
	$NbTe_2$	1.9	Compacted polycrystalline	[105]
	TaS_2	5	Bulk material	[107]
2D	$TaSe_2$	16	Bulk material	[107,108]
	$TaSe_2$	1.7	Compacted polycrystalline	[105]
	$TaTe_2$	1.4	Compacted polycrystalline	[105]
	TiS_2	6.8, 4.2	In plane and out of plane	[109]
	WSe_2	1.7	Compacted polycrystalline	[105]
	WS_2	2.2	Pristine	[104]
	WSe_2	0.8	Pristine	[104]
	WTe_2	1.6	Compacted polycrystalline	[105]
	$ZrSe_2$	10	First-principles study	[103]
	ZrS_2	18	First-principles study	[103]

at higher temperatures when the phonon-phonon scattering mechanism starts to dominate. At $T = 200$ K, the experimental and calculated values are 6.62 and 9.11 $W\,m^{-1}\,K^{-1}$, respectively. From the experimental side, the accuracy of PTC technique to handle chain-structures, such as $TaSe_3$ is under question [89]. Missing from the calculations are the effects of impurities, surface scattering, finite grain sizes, and random isotopes [92]. For $ZrTe_3$, there is one reported measurement of the thermal conductivity in a bulk polycrystalline sample with a value of 7 $W\,m^{-1}\,K^{-1}$ at room temperature which is similar to our calculated value of 9 $W\,m^{-1}\,K^{-1}$.

Order-of-magnitude estimates of the electronic components of the thermal conductivities can be obtained from the Wiedemann-Franz law using the Sommerfeld value of the Lorenz number $2.44 \times 10^{-8}\,W\,\Omega\,K^{-2}$. Values for the Lorenz number do vary, but for room-temperature metals, they tend to lie within a range of 0.6–2 times the Sommerfeld value [93]. Using the values for the electrical conductivities from Sec. II, the estimated room-temperature electrical component of the thermal conductivity along the chain direction for $TaSe_3$ is 1.2 $Wm^{-1}\,K^{-1}$. For $ZrTe_3$, the estimated room-temperature electrical component of the thermal conductivity along the chain direction ranges from 2.9 to 5.1 $Wm^{-1}\,K^{-1}$, and along the cross-chain direction, it ranges from 4.1 to 5.1 $Wm^{-1}\,K^{-1}$. For comparison, the corresponding values of the room-temperature lattice thermal conductivities for $TaSe_3$ and $ZrTe_3$ along the chain direction are 6.2 and 9.6 $Wm^{-1}\,K^{-1}$, respectively, and for $ZrTe_3$ along the cross chain direction, it is 3.9 $Wm^{-1}\,K^{-1}$. Thus, the Wiedemann-Franz law with the Sommerfeld approximation for the Lorenz number gives room-temperature electrical components of the thermal conductivities that are on the same order as the lattice components.

To understand the contribution of the phonon modes and frequencies to the lattice thermal conductivity, we consider the room-temperature, normalized thermal conductivity as a cumulative function of phonon frequency in Fig. 3. In $TaSe_3$, 50% of the thermal conductivity in the chain direction (κ_{yy}) is contributed by modes with frequencies below 75 cm^{-1}. The thermal conductivity on the *a*-*c* plane has a larger contribution from lower-frequency phonons. In the cross-chain direction, 50% of κ_{cc} is contributed by modes with frequencies below 64 cm^{-1}, and in the cross-plane direction, 50% of κ_{cp} is contributed by modes with frequencies below 36 cm^{-1}.

In $ZrTe_3$, the heat is carried by lower-frequency phonons than in $TaSe_3$. In $ZrTe_3$, 50% of thermal conductivity along both the chain direction (κ_{yy}) and the cross-chain direction (κ_{cc}) is contributed by phonons with frequencies below 52 cm^{-1}. In the cross-plane direction 50% of κ_{cp} is contributed by modes with frequencies below 26 cm^{-1}.

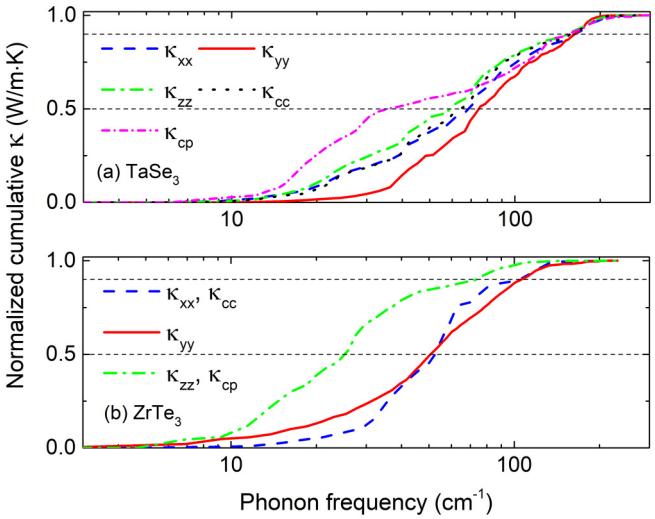

FIG. 3. Thermal conductivity values at $T = 300$ K, normalized to their maximum values along various crystallographic directions as cumulative functions of the phonon frequency for (a) $TaSe_3$ and (b) $ZrTe_3$. For $ZrTe_3$, the values for the cc and cp directions are indistinguishable from the values for κ_{xx} and κ_{zz}, respectively. Reference horizontal lines are at 0.5 and 0.9.

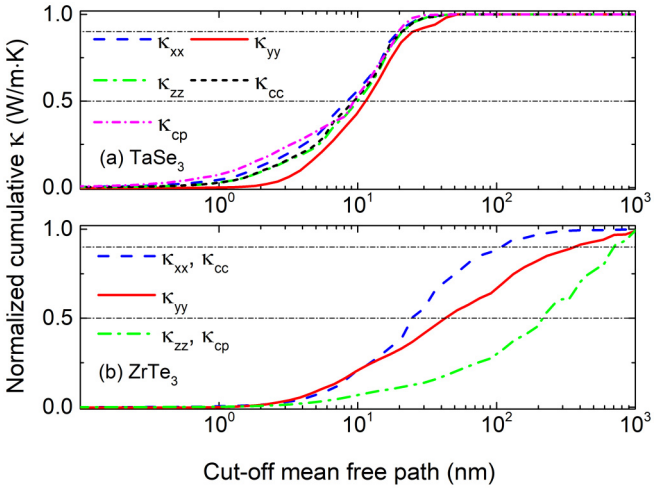

FIG. 4. Thermal conductivity values at $T = 300$ K, normalized to its maximum value along various crystallographic directions, as functions of the cutoff mean free path for (a) $TaSe_3$ and (b) $ZrTe_3$. Reference horizontal lines are at 0.5 and 0.9.

For both of these materials, a significant percentage of the heat at room temperature is carried by the optical modes. This phenomenon has also recently been observed in TiS_3 [70]. Consider the chain direction Γ-Y. In $TaSe_3$, essentially all of the modes above 75 cm^{-1} are optical modes as can be seen in Fig. 1(e). Thus, approximately 50% of the heat in $TaSe_3$ at room temperature is carried by optical modes. In $ZrTe_3$, the spectrum along the chain direction above 64 cm^{-1} is composed primarily of optical modes, and it carries 33% of the heat.

Another way to analyze the physics of the heat current carried by phonons is to calculate the normalized κ as a function of the cutoff mean free path. The results are shown in Fig. 4. For $TaSe_3$, 90% of the thermal conductivity in the chain direction is carried by phonons with a mean free path of 25 nm or less. In both the cross-chain and the cross-plane directions 90% of the thermal conductivity is carried by phonons with mean free paths of 21 nm or less. The corresponding cutoff mean free paths for $ZrTe_3$ are approximately an order of magnitude greater. For $ZrTe_3$, in the chain, cross-chain, and cross-plane directions, 90% of the heat is carried by phonons with mean free paths less than or equal to 365, 110, and 700 nm, respectively.

To obtain a representative mean free path (λ_R) of heat-carrying phonons, the cumulative κ with respect to the cutoff mean free path (λ_{max}) in Fig. 4, is fitted to a single parametric function [84,94],

$$\kappa(\lambda_{max}) = \frac{\kappa_0}{1 + \lambda_R/\lambda_{max}}, \tag{4}$$

where κ_0 is the maximum thermal conductivity. The values for λ_R for the different transport directions are tabulated in Table III. They correspond closely to the cutoff mean free paths in Fig. 4 that account for 50% of the thermal conductivity in each direction. These values serve as indicators as to how and when the thermal conductivity will be affected by geometrical scaling. When dimensions are reduced below λ_R, the thermal conductivity will be reduced. The representative mean free path (λ_R) for $TaSe_3$ is lower than that of $ZrTe_3$ as shown in Table III. This is consistent with the fact that, in the low-frequency (0–50 cm^{-1}) region, the phonon-scattering lifetimes in $TaSe_3$ are approximately one order of magnitude shorter than those of $ZrTe_3$ as discussed below and shown in Figs. 5(c) and 5(d). The cross-plane thermal conductivity of $ZrTe_3$ has the longest representative mean free path of 178 cm^{-1}. This is consistent with the fact that the phonons contributing to the cross-plane thermal conductivity are very low frequency (50% of the heat is carried by phonons with frequencies below 25 cm^{-1}). This frequency range is well below the optical branches so that three-phonon scattering is strongly restricted by energy and momentum conservation.

To gain further insight into why there is a significant difference between the thermal conductivity in these materials, we inspect the phonon velocity as well as the phonon lifetimes of the thermal modes. Figures 5(a) and 5(b) show the absolute velocity distributions of the heat-carrying phonons for each phonon mode inside the irreducible BZ, and the reference horizontal lines are at 4 km/s. The lifetimes are shown in Figs. 5(c) and 5(d), and the reference horizontal lines are at 100 ps. In the low-frequency range $\lesssim$50 cm^{-1}, $ZrTe_3$

TABLE III. Representative mean free path (λ_R) of heat carrying phonons in $TaSe_3$ and $ZrTe_3$, at $T = 300$ K in the three directions indicated in the header.

	λ_R (nm)				
	x	y	z	Cross-chain	Cross-plane
$TaSe_3$	7.3	10.6	8.5	8.2	7.1
$ZrTe_3$	25.3	43.7	178	25.3	178

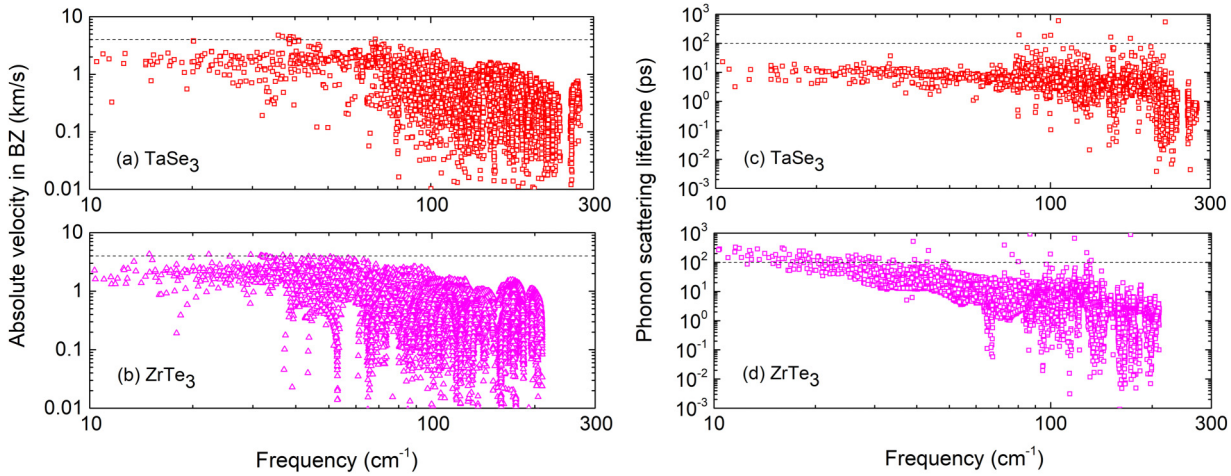

FIG. 5. Absolute velocity of phonon modes in the irreducible Brillouin zone of (a) $TaSe_3$ and (b) $ZrTe_3$. The reference horizontal lines are at 4 km/s. Scattering lifetimes of the phonon modes at $T = 300$ K for (c) $TaSe_3$ and (d) $ZrTe_3$. The reference horizontal lines are at 100 ps.

has higher velocity phonons with longer lifetimes than those of $TaSe_3$.

In this low-frequency range, the phonon lifetimes of $ZrTe_3$ are approximately one order of magnitude longer than those of $TaSe_3$. For $ZrTe_3$, the optical modes are close to or above 50 cm^{-1}. For $TaSe_3$, there are several optical branches that fall below 50 cm^{-1} accompanied by a number of band crossings and anticrossings. Also, since the unit cell of $TaSe_3$ is twice as large on the a-c plane as that of $ZrTe_3$, there are features in the acoustic dispersion along Γ-X and Γ-Z that resemble zone folding in which the acoustic branches fold back at the zone boundary and return to Γ. Both of these features result in a greater number of channels for low-frequency phonon relaxation in $TaSe_3$ compared to those in $ZrTe_3$ and correspondingly lower phonon lifetimes. A simple illustration of how zone folding opens new phonon relaxation channels is shown in Ref. [95].

V. SUMMARY AND CONCLUSION

The phonon dispersions and lattice thermal conductivities of $TaSe_3$ and $ZrTe_3$ are determined using density functional theory and the phonon BTE. The anisotropy of the LA acoustic phonons as characterized by the ratios of the chain, cross-chain, and cross-plane velocities, is considerably larger in $TaSe_3$ than in $ZrTe_3$. The anisotropy of the maximum velocities of the TA modes is always less. The maximum LA velocity in $ZrTe_3$ occurs in the cross-chain direction, and this is consistent with the strong cross-chain bonding that gives rise to large Fermi velocities.

However, the thermal conductivity for both crystals is maximum in the chain direction. The thermal conductivity of $ZrTe_3$ is larger than that of $TaSe_3$ in each of the three directions: chain, cross-chain, and cross-plane; and it is considerably more isotropic. For $TaSe_3$ ($ZrTe_3$), the room-temperature diagonal thermal conductivity values in the three directions are $\kappa_{yy} = 6.2$ (9.6), $\kappa_{cc} = 0.80$ (3.9), and $\kappa_{cp} = 0.13$ (2.3) W m^{-1} K^{-1}.

A significant percentage of the heat at room temperature is carried by the optical phonons. In $TaSe_3$, the spectrum along the chain direction above 75 cm^{-1} is composed of the optical branches, and this part of the spectrum carries 50% of the heat at room temperature. In $ZrTe_3$, the spectrum along the chain direction above 64 cm^{-1} is composed primarily of optical branches, and it carries 33% of the heat at room temperature. For $TaSe_3$ ($ZrTe_3$) along the chain direction at $T = 300$ K, 50% of the heat is carried by phonons below 75 (50) cm^{-1}, and this part of the phonon spectra consists primarily of the acoustic branches.

The differences between the two materials in their phonon velocities and lifetimes are most apparent in the lowfrequency range of $\lesssim$50 cm^{-1}. In this frequency range, the maximum phonon velocities of $ZrTe_3$ are approximately a factor of 2 greater than those of $TaSe_3$, and the phonon lifetimes in $ZrTe_3$ are approximately an order of magnitude greater than those in $TaSe_3$. The longer lifetimes result in considerably longer mean free paths in $ZrTe_3$ compared to those in $TaSe_3$. The representative mean free paths in the chain, cross-chain, and cross-plain directions for $TaSe_3$ ($ZrTe_3$) are 10.6 (43.7), 8.2 (25.3), and 7.1 (178) nm, respectively. The shorter lifetimes in the low-frequency range of $TaSe_3$ are consistent with the presence of optical branches and zone-folding features of the acoustic branches that arise due to the doubling of the $TaSe_3$ unit cell on the a-c plane compared to the unit cell of $ZrTe_3$. Both of these features serve to introduce more scattering channels for low-frequency phonon relaxation.

ACKNOWLEDGMENTS

This work was supported, in part, by the NSF under Grant No. EFRI-1433395. Calculations of $ZrTe_3$ were supported, in part, by Spins and Heat in Nanoscale Electronic Systems (SHINES) an Energy Frontier Research Center funded by the U.S. Department of Energy, Office of Science, Basic Energy Sciences under Award No. DE-SC0012670. This work used the Extreme Science and Engineering Discovery Environment (XSEDE) [96], which is supported by National Science Foundation Grant No. ACI-1548562 and Allocation ID TG-DMR130081.

APPENDIX: ADDITIONAL TABLES AND FIGURES

The calculated and experimental lattice constants and angles for $TaSe_3$ and $ZrTe_3$ are provided in Table IV.The room-temperature values of the diagonal elements of the thermal conductivity tensors calculated from the RTA and the full iterative approaches are listed in Table V, and the comparison for all temperatures is shown in Fig. 6. The fitting coefficients for the temperature-dependent thermal conductivities $\kappa(T) = c_1 + c_2 T^{-1}$ are provided in Table VI, and the plot showing the quality of the fits is given in Fig. 7. Electronic structure plots for $TaSe_3$ and $ZrTe_3$ are shown in Fig. 8. The convergence of the lattice thermal conductivities for different q-point grids is shown in Fig. 9.

TABLE IV. Lattice constants (Å) and angles (degrees) for $TaSe_3$ and $ZrTe_3$. The values labeled "This paper" are the values obtained after structure relaxation. The experimental values in the corresponding literature were obtained at room temperature.

Crystal	Remark	a	b	c	α	β	γ
$TaSe_3$	This paper	10.452	3.508	9.875	90	106.36	90
	Experiment [73,97]	10.411	3.494	9.836	90	106.36	90
$ZrTe_3$	This paper	5.915	3.882	10.152	90	97.94	90
	Experiment [98]	5.895	3.926	10.104	90	97.93	90

TABLE V. Diagonal elements of the lattice thermal conductivity tensors calculated from the RTA and iterative methods at $T = 300$ K.

	Method	κ_{xx}	κ_{yy}	κ_{zz}
$TaSe_3$	RTA	0.3718	4.0423	0.5644
	Iterative	0.3722	6.1522	0.5643
$ZrTe_3$	RTA	3.6621	8.2807	2.2823
	Iterative	3.8764	9.5748	2.3435

TABLE VI. Fitting coefficients c_1 (W m^{-1} K^{-1}) and c_2 (W m^{-1}) for the temperature dependence of the diagonal elements of κ for $TaSe_3$ and $ZrTe_3$ given by the expression $\kappa = c_1 + c_2 T^{-1}$. For $TaSe_3$, the coefficients for κ_{cc} and κ_{cp} are also shown. For $ZrTe_3$, these are the same as κ_{xx} and κ_{zz}, respectively.

	Coefficient	κ_{xx}	κ_{yy}	κ_{zz}	κ_{cc}	κ_{cp}
$TaSe_3$	c_1	0.003989	−0.02828	−0.003387	−0.001137	0.001768
	c_2	110.4	1880.0	171.9	243.2	39.10
$ZrTe_3$	c_1	−0.1578	−0.1457	−0.1441		
	c_2	1241	2956	772.3		

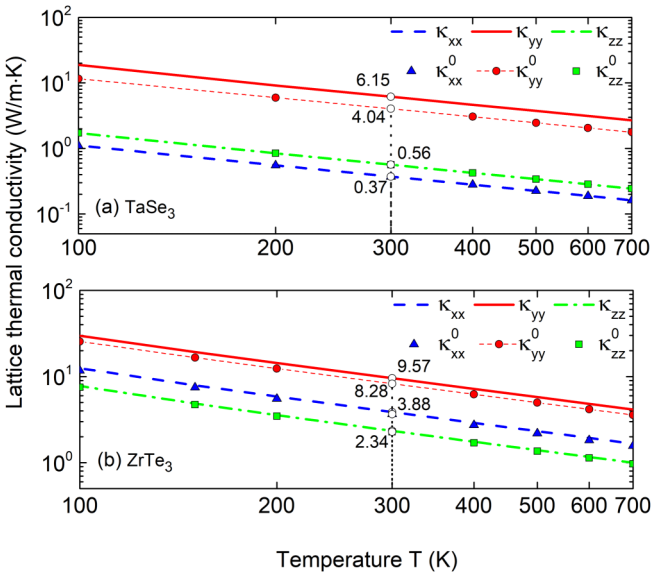

FIG. 6. Lattice thermal conductivities of (a) $TaSe_3$ and (b) $ZrTe_3$ calculated from the RTA and iterative approaches as indicated by the legends. The curves labeled κ^0 are calculated using the RTA, and the curves labeled κ are calculated from the full iterative method.

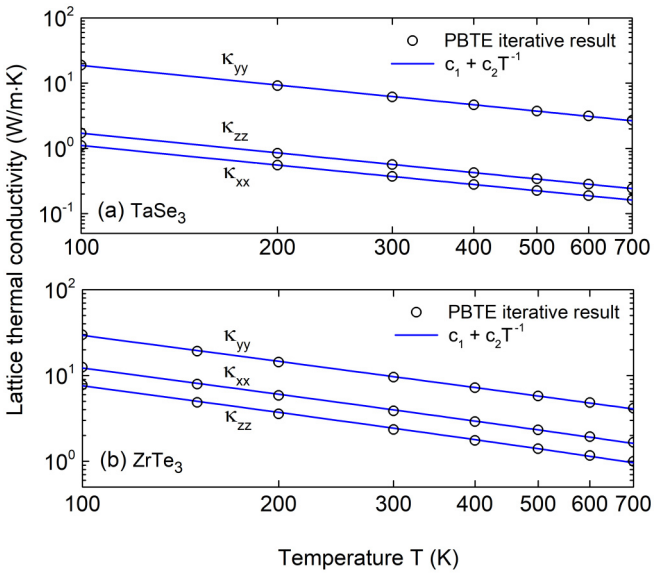

FIG. 7. Fitted thermal conductivities for (a) $TaSe_3$ and (b) $ZrTe_3$ using the coefficients listed in Table VI. The circles show the numerically calculated values, and the solid lines show the analytical fits.

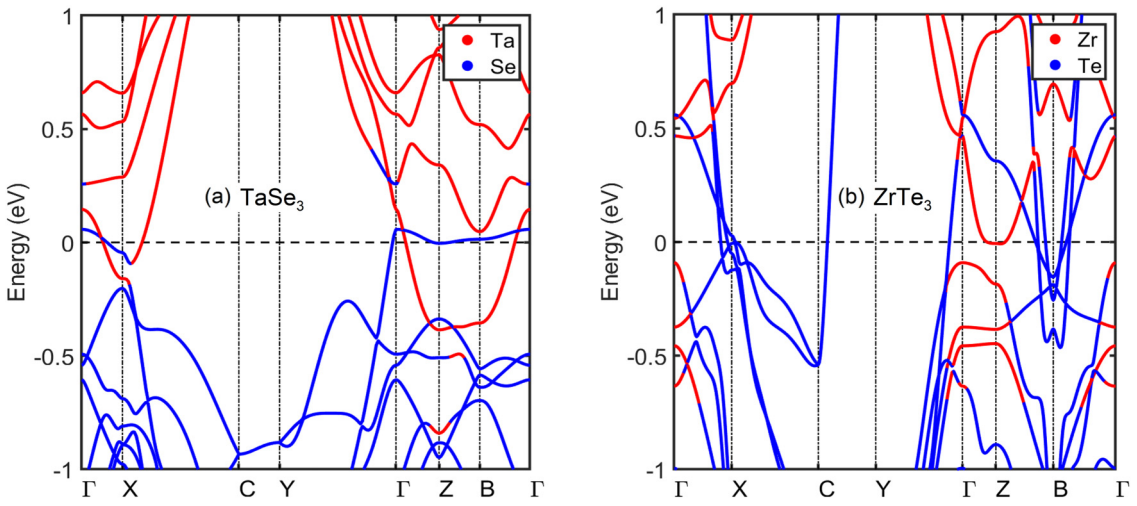

FIG. 8. Electronic structure of (a) $TaSe_3$ and (b) $ZrTe_3$. The color indicates the dominant orbital contributions from the metal or chalcogen atoms.

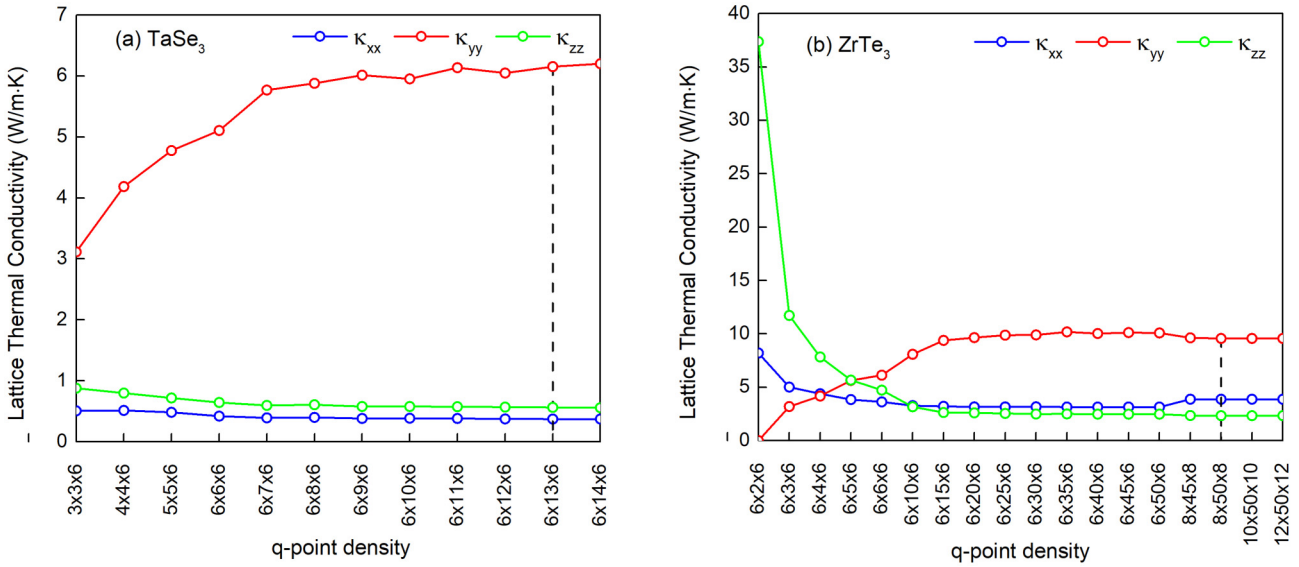

FIG. 9. Lattice thermal conductivity for (a) $TaSe_3$ and (b) $ZrTe_3$ for different q-point grids at $T = 300$ K. For our calculation we have chosen a q point of $6 \times 13 \times 6$ and $8 \times 50 \times 8$ for $TaSe_3$ and $ZrTe_3$, respectively. The change in thermal conductivity beyond this q point is negligible and below 1%.

[1] D. W. Bullett, J. Phys. C: Solid State Phys. **12**, 277 (1979).
[2] S. K. Srivastava and B. N. Avasthi, J. Mater. Sci. **27**, 3693 (1992).
[3] J. O. Island, A. J. Molina-Mendoza, M. Barawi, R. Biele, E. Flores, J. M. Clamagirand, J. R. Ares, C. Sánchez, H. S. J. van der Zant, R. D'Agosta, I. J. Ferrer, and A. Castellanos-Gomez, 2D Mater. **4**, 022003 (2017).
[4] S. Furuseth, L. Brattas, and A. Kjekshus, Acta Chem. Scand. A **29**, 623 (1975).
[5] K. Endo, H. Ihara, S. Gonda, and K. Watanabe, Physica B+C **105**, 159 (1981).
[6] M. H. Rashid and D. J. Sellmyer, Phys. Rev. B **29**, 2359 (1984).
[7] Y. Jin, X. Li, and J. Yang, Phys. Chem. Chem. Phys. **17**, 18665 (2015).
[8] J. Dai and X. C. Zeng, Angew. Chem., Int. Ed. **54**, 7572 (2015).
[9] J. O. Island, R. Biele, M. Barawi, J. M. Clamagirand, J. R. Ares, C. Sánchez, H. S. J. van der Zant, I. J. Ferrer, R. D'Agosta, and A. Castellanos-Gomez, Sci. Rep. **6**, 22214 (2016).
[10] A. Pant, E. Torun, B. Chen, S. Bhat, X. Fan, K. Wu, D. P. Wright, F. M. Peeters, E. Soignard, H. Sahin *et al.*, Nanoscale **8**, 16259 (2016).
[11] J. Dai, M. Li, and X. C. Zeng, Wiley Interdiscip. Rev. Comput. Mol. Sci. **6**, 211 (2016).
[12] W. Kong, C. Bacaksiz, B. Chen, K. Wu, M. Blei, X. Fan, Y. Shen, H. Sahin, D. Wright, D. S. Narang *et al.*, Nanoscale **9**, 4175 (2017).
[13] T. Sambongi, M. Yamamoto, K. Tsutsumi, Y. Shiozaki, K. Yamaya, and Y. Abe, J. Phys. Soc. Jpn. **42**, 1421 (1977).
[14] P. Haen, F. Lapierre, P. Monceau, M. N. nez Regueiro, and J. Richard, Solid State Commun. **26**, 725 (1978).
[15] M. Yamamoto, J. Phys. Soc. Jpn. **45**, 431 (1978).
[16] K. Yamaya, S. Takayanagi, and S. Tanda, Phys. Rev. B **85**, 184513 (2012).
[17] G. Grüner, Rev. Mod. Phys. **60**, 1129 (1988).
[18] G. Grüner, *Density Waves in Solids* (Perseus, Boston, 1994).
[19] P. Monceau, Adv. Phys. **61**, 325 (2012).
[20] V. Y. Pokrovskii, S. G. Zybtsev, M. V. Nikitin, I. G. Gorlova, V. F. Nasretdinova, and S. V. Zaitsev-Zotov, Phys.-Usp. **56**, 29 (2013).
[21] R. M. Fleming, D. E. Moncton, and D. B. McWhan, Phys. Rev. B **18**, 5560 (1978).
[22] M. E. Itkis, F. Y. Nad, and P. Monceau, J. Phys.: Condens. Matter **2**, 8327 (1990).
[23] S. G. Zybtsev, V. Y. Pokrovskii, V. F. Nasretdinova, S. V. Zaitsev-Zotov, V. V. Pavlovskiy, A. B. Odobesco, W. W. Pai, M.-W. Chu, Y. G. Lin, E. Zupanič, H. J. P. van Midden, S. Šturm, E. Tchernychova, A. Prodan, J. C. Bennett, I. R. Mukhamedshin, O. V. Chernysheva, A. P. Menushenkov, V. B. Loginov, B. A. Loginov, A. N. Titov, and M. Abdel-Hafiez, Phys. Rev. B **95**, 035110 (2017).
[24] A. Zettl and G. Grüner, Phys. Rev. B **26**, 2298 (1982).
[25] R. P. Hall, M. F. Hundley, and A. Zettl, Phys. Rev. B **38**, 13002 (1988).
[26] J. Bardeen, E. Ben-Jacob, A. Zettl, and G. Grüner, Phys. Rev. Lett. **49**, 493 (1982).
[27] A. Zettl, C. M. Jackson, and G. Grüner, Phys. Rev. B **26**, 5773 (1982).
[28] R. E. Thorne, W. G. Lyons, J. W. Lyding, J. R. Tucker, and J. Bardeen, Phys. Rev. B **35**, 6360 (1987).
[29] H. S. J. van der Zant, E. Slot, S. V. Zaitsev-Zotov, and S. N. Artemenko, Phys. Rev. Lett. **87**, 126401 (2001).
[30] S. G. Zybtsev, V. Y. Pokrovskii, V. F. Nasretdinova, and S. V. Zaitsev-Zotov, Appl. Phys. Lett. **94**, 152112 (2009).
[31] S. V. Zaitsev-Zotov, Phys.-Usp. **47**, 533 (2004).

[32] J. McCarten, D. A. DiCarlo, M. P. Maher, T. L. Adelman, and R. E. Thorne, Phys. Rev. B **46**, 4456 (1992).

[33] H. S. J. van der Zant, A. Kalwij, O. C. Mantel, N. Markovic, Y. I. Latyshev, B. Pannetier, and P. Monceau, J. Phys. IV France **9**, Pr10-157 (1999).

[34] H. S. J. van der Zant, N. Markovic, and E. Slot, Physics-Uspekhi **44**, 61 (2001).

[35] E. Slot, H. S. J. van der Zant, K. O'Neill, and R. E. Thorne, Phys. Rev. B **69**, 073105 (2004).

[36] K. Inagaki, T. Toshima, S. Tanda, and K. Yamaya, Appl. Phys. Lett. **86**, 073101 (2005).

[37] Y. S. Hor, Z. L. Xiao, U. Welp, Y. Ito, J. F. Mitchell, R. E. Cook, W. K. Kwok, and G. W. Crabtree, Nano Lett. **5**, 397 (2005).

[38] S. G. Zybtsev and V. Y. Pokrovskii, Phys. Rev. B **84**, 085139 (2011).

[39] S. Bhattacharya, A. N. Bloch, and J. P. Stokes, Frequency Modulator Using Material Having Sliding Charge Density Waves, U.S. Patent No. 4,580,110 (1 April 1986).

[40] T. L. Adelman, S. V. Zaitsev-Zotov, and R. E. Thorne, Phys. Rev. Lett. **74**, 5264 (1995).

[41] G. Blumberg and P. B. Littlewood, Electronic devices based on density wave dielectrics, U.S. Patent No. 6,735,073 (11 May 2004).

[42] D. Mihailovic, D. Dvorsek, V. V. Kabanov, J. Demsar, L. Forró, and H. Berger, Appl. Phys. Lett. **80**, 871 (2002).

[43] K. Stöwe and F. R. Wagner, J. Solid State Chem. **138**, 160 (1998).

[44] R. Seshardi, E. Suard, C. Felser, E. W. Finckh, A. Maignan, and W. Tremel, J. Mater. Chem. **8**, 2869 (1998).

[45] C. Felser, E. W. Finckh, H. Kleinke, F. Rocker, and W. Tremel, J. Mater. Chem. **8**, 1787 (1998).

[46] T. Yokoya, T. Kiss, A. Chainani, S. Shin, and K. Yamaya, Phys. Rev. B **71**, 140504(R) (2005).

[47] M. Hoesch, A. Bosak, D. Chernyshov, H. Berger, and M. Krisch, Phys. Rev. Lett. **102**, 086402 (2009).

[48] M. Hoesch, X. Cui, K. Shimada, C. Battaglia, S.-i. Fujimori, and H. Berger, Phys. Rev. B **80**, 075423 (2009).

[49] Y. Hu, F. Zheng, X. Ren, J. Feng, and Y. Li, Phys. Rev. B **91**, 144502 (2015).

[50] S. L. Gleason, Y. Gim, T. Byrum, A. Kogar, P. Abbamonte, E. Fradkin, G. J. MacDougall, D. J. Van Harlingen, X. Zhu, C. Petrovic, and S. L. Cooper, Phys. Rev. B **91**, 155124 (2015).

[51] A. M. Ganose, L. Gannon, F. Fabrizi, H. Nowell, S. A. Barnett, H. Lei, X. Zhu, C. Petrovic, D. O. Scanlon, and M. Hoesch, Phys. Rev. B **97**, 155103 (2018).

[52] M. Hoesch, L. Gannon, K. Shimada, B. J. Parrett, M. D. Watson, T. K. Kim, X. Zhu, and C. Petrovic, Phys. Rev. Lett. **122**, 017601 (2019).

[53] L. Yue, S. Xue, J. Li, W. Hu, A. Barbour, F. Zheng, L. Wang, J. Feng, S. B. Wilkins, C. Mazzoli *et al.*, Nat. Commun. **11**, 98 (2020).

[54] A. Patra and C. S. Rout, RSC Adv. **10**, 36413 (2020).

[55] J. O. Island, M. Buscema, M. Barawi, J. M. Clamagirand, J. R. Ares, C. Sánchez, I. J. Ferrer, G. A. Steele, H. S. J. van der Zant, and A. Castellanos-Gomez, Adv. Opt. Mater. **2**, 641 (2014).

[56] J. O. Island, M. Barawi, R. Biele, A. Almazán, J. M. Clamagirand, J. R. Ares, C. Sánchez, H. S. J. van der Zant, J. V. Álvarez, R. D'Agosta, I. J. Ferrer, and A. Castellanos-Gomez, Adv. Mater. **27**, 2595 (2015).

[57] A. Lipatov, P. M. Wilson, M. Shekhirev, J. D. Teeter, R. Netusil, and A. Sinitskii, Nanoscale **7**, 12291 (2015).

[58] S. J. Gilbert, A. Lipatov, A. J. Yost, M. J. Loes, A. Sinitskii, and P. A. Dowben, Appl. Phys. Lett. **114**, 101604 (2019).

[59] M. Randle, A. Lipatov, A. Kumar, C.-P. Kwan, J. Nathawat, B. Barut, S. Yin, K. He, N. Arabchigavkani, R. Dixit, T. Komesu, J. Avila, M. C. Asensio, P. A. Dowben, A. Sinitskii, U. Singisetti, and J. P. Bird, ACS Nano **13**, 803 (2019).

[60] N. Papadopoulos, E. Flores, K. Watanabe, T. Taniguchi, J. R. Ares, C. Sanchez, I. J. Ferrer, A. Castellanos-Gomez, G. A. Steele, and H. S. J. van der Zant, 2D Mater. **7**, 015009 (2019).

[61] M. Abdulsalam and D. P. Joubert, Eur. Phys. J. B **88**, 177 (2015).

[62] E. Zhang, P. Wang, Z. Li, H. Wang, C. Song, C. Huang, Z.-G. Chen, L. Yang, K. Zhang, S. Lu *et al.*, ACS Nano **10**, 8067 (2016).

[63] H. Yuan, X. Liu, F. Afshinmanesh, W. Li, G. Xu, J. Sun, B. Lian, A. G. Curto, G. Ye *et al.*, Nat. Nanotechnol. **10**, 707 (2015).

[64] M. A. Stolyarov, G. Liu, M. A. Bloodgood, E. Aytan, C. Jiang, R. Samnakay, T. T. Salguero, D. L. Nika, S. L. Rumyantsev, M. S. Shur, K. N. Bozhilov, and A. A. Balandin, Nanoscale **8**, 15774 (2016).

[65] A. Geremew, M. Bloodgood, E. Aytan, B. Woo, S. Corber, G. Liu, K. Bozhilov, T. Salguero, S. Rumyantsev, M. Rao *et al.*, IEEE Electron Device Lett. **39**, 735 (2018).

[66] T. A. Empante, A. Martinez, M. Wurch, Y. Zhu, A. K. Geremew, K. Yamaguchi, M. Isarraraz, S. Rumyantsev, E. J. Reed, A. A. Balandin, and L. Bartels, Nano Lett. **19**, 4355 (2019).

[67] M. Dresselhaus, G. Dresselhaus, X. Sun, Z. Zhang, S. Cronin, and T. Koga, Phys. Solid State **41**, 679 (1999).

[68] Z. Zhou, H. Liu, D. Fan, G. Gao, and C. Sheng, ACS Appl. Mater. Interfaces **10**, 37031 (2018).

[69] M. Hooda, T. Tripathi, and C. Yadav, J. Alloys Compd. **785**, 603 (2019).

[70] H. Liu, X. Yu, K. Wu, Y. Gao, S. Tongay, A. Javey, L. Chen, J. Hong, and J. Wu, Nano Lett. **20**, 5221 (2020).

[71] T. Wieting, A. Grisel, and F. Levy, Mol. Cryst. Liq. Cryst. **81**, 117 (1982).

[72] A. Zwick, M. A. Renucci, and A. Kjekshus, J. Phys. C **13**, 5603 (1980).

[73] E. Bjerkelund and A. Kjekshus, Acta Chem. Scared **19**, 701 (1965).

[74] H. Nakajima, K. Nomura, and T. Sambongi, Physica B+C **143**, 240 (1986).

[75] S. Takahashi, T. Sambongi, J. Brill, and W. Roark, Solid State Commun. **49**, 1031 (1984).

[76] K. Yamaya and G. Oomi, J. Phys. Soc. Jpn. **51**, 3512 (1982).

[77] P. E. Blöchl, Phys. Rev. B **50**, 17953 (1994).

[78] J. P. Perdew, K. Burke, and M. Ernzerhof, Phys. Rev. Lett. **77**, 3865 (1996).

[79] G. Kresse and J. Hafner, Phys. Rev. B **48**, 13115 (1993).

[80] G. Kresse and J. Furthmüller, Comput. Mater. Sci. **6**, 15 (1996).

[81] S. Grimme, J. Comput. Chem. **27**, 1787 (2006).

[82] A. Togo, F. Oba, and I. Tanaka, Phys. Rev. B **78**, 134106 (2008).
[83] A. Togo and I. Tanaka, Scr. Mater. **108**, 1 (2015).
[84] W. Li, J. Carrete, N. A. Katcho, and N. Mingo, Comput. Phys. Commun. **185**, 1747 (2014).
[85] W. Li and N. Mingo, Phys. Rev. B **91**, 144304 (2015).
[86] W. Li, N. Mingo, L. Lindsay, D. A. Broido, D. A. Stewart, and N. A. Katcho, Phys. Rev. B **85**, 195436 (2012).
[87] See Supplemental Material at http://link.aps.org/supplemental/10.1103/PhysRevMaterials.5.034010 for the experimental and calculated values.
[88] T. J. Wieting, A. Grisel, F. Lévy, and P. Schmid, *Phonon studies of chemical bonding in the IVB and VB trichalcogenides*, *Quasi One-Dimensional Conductors I*, Lecture Notes in Physics Vol. 95 (Springer-Verlag, Berlin, 1979), pp. 354–358.
[89] B. Zawilski, R. L. IV, N. Lowhorn, and T. Tritt, Solid State Commun. **150**, 1299 (2010).
[90] M. Yao, M. Zebarjadi, and C. P. Opeil, J. Appl. Phys. **122**, 135111 (2017).
[91] B. M. Zawilski, R. T. Littleton, and T. M. Tritt, Rev. Sci. Instrum. **72**, 1770 (2001).
[92] L. Lindsay, D. A. Broido, and T. L. Reinecke, Phys. Rev. B **88**, 144306 (2013).
[93] G. S. Kumar, G. Prasad, and R. O. Pohl, J. Mater. Sci. **28**, 4261 (1993).
[94] H. Wang, Y. Gao, and G. Liu, RSC Adv. **7**, 8098 (2017).
[95] H. Li, H. Ying, X. Chen, D. L. Nika, A. I. Cocemasov, W. Cai, A. A. Balandin, and S. Chen, Nanoscale **6**, 13402 (2014).
[96] J. Towns, T. Cockerill, M. Dahan, I. Foster, K. Gaither, A. Grimshaw, V. Hazlewood, S. Lathrop, D. Lifka, G. D. Peterson *et al.*, Comput. Sci. Eng. **16**, 62 (2014).
[97] E. Bjerkelund and A. Kjekshus, Z. Anorg. Allg. Chem. **328**, 235 (1964).
[98] H. Furuseth and S. Fjellvag, Acta Chem. Scandin **45**, 694 (1991).
[99] J. Brill, C. Tzou, G. Verma, and N. Ong, Solid State Commun. **39**, 233 (1981).
[100] A. Smontara and K. Biljakovic, Mol. Cryst. Liq. Cryst. **121**, 141 (1985).
[101] J. Zhu, T. Feng, S. Mills, P. Wang, X. Wu, L. Zhang, S. T. Pantelides, X. Du, and X. Wang, ACS Appl. Mater. Interfaces **10**, 40740 (2018).
[102] M. K. Hooda and C. S. Yadav, Appl. Phys. Lett. **111**, 053902 (2017).
[103] G. Yumnam, T. Pandey, and A. K. Singh, J. Chem. Phys. **143**, 234704 (2015).
[104] J.-Y. Kim, S. M. Choi, W.-S. Seo, and W.-S. Cho, Bull. Korean Chem. Soc. **31**, 3225 (2010).
[105] L. Brixner, J. Inorg. Nucl. Chem. **24**, 257 (1962).
[106] Y. Nishio, J. Phys. Soc. Jpn. **63**, 223 (1994).
[107] M. D. Núñez-Regueiro, J. M. Lopez-Castillo, and C. Ayache, Phys. Rev. Lett. **55**, 1931 (1985).
[108] Z. Yan, C. Jiang, T. R. Pope, C. F. Tsang, J. L. Stickney, P. Goli, J. Renteria, T. T. Salguero, and A. A. Balandin, J. Appl. Phys. **114**, 204301 (2013).
[109] H. Imai, Y. Shimakawa, and Y. Kubo, Phys. Rev. B **64**, 241104(R) (2001).